coatings

MDPI

Article

Fabrication of Luminescent Antireflective Coatings with $CaMoO_4:Eu^{3+}$/Ag Composite Structure

Kazuhiro Matsumoto, Manabu Hagiwara and Shinobu Fujihara *

Department of Applied Chemistry, Faculty of Science and Technology, Keio University, 3-14-1 Hiyoshi, Kohoku-ku, Yokohama 223-8522, Japan; mk.91h3@gmail.com (K.M.); hagiwara@applc.keio.ac.jp (M.H.)
* Correspondence: shinobu@applc.keio.ac.jp; Tel.: +81-45-566-1581

Academic Editor: Pascal Buskens
Received: 10 April 2017; Accepted: 31 May 2017; Published: 2 June 2017

Abstract: Highly transparent and luminescent $CaMoO_4:Eu^{3+}$/Ag composite films were fabricated on glass substrates as multifunctional antireflective (AR) coatings. The films were deposited through a combination of a sol–gel dip-coating technique and a hot water treatment. With the addition of an aluminum source in coating solutions, the sol–gel-derived films underwent a remarkable microstructural change during the hot water treatment due to the reaction between an amorphous alumina phase and water. This change brought both an antireflective effect (suppression of Fresnel reflection) and luminescence enhancement (suppression of total internal reflection) to the films. The introduction of Ag nanoparticles into the films further increased luminescence intensity without losing the antireflective effect.

Keywords: antireflective coatings; photoluminescence; nanocomposite; sol–gel method; calcium molybdate; europium; silver nanoparticles

1. Introduction

Solid-state luminescent materials (phosphors) are commonly composed of wide band-gap inorganic compounds, and hence do not absorb visible light. Thin-film phosphors are therefore optically transparent in the visible light region, as their microstructure is designed to have less light scattering. Transparent thin-film phosphors are used in various applications such as X-ray imaging devices [1], spectral converters for photovoltaic devices [2], light-emitting devices [3,4], and so on. A family of the tungstate and the molybdate compounds with a general formula of AMO_4 (A = Ca, Sr, Ba, and M = W, Mo) has attracted much attention for use as unique optical materials such as laser hosts, phosphors, and scintillators [5–7]. Among them, $CaMoO_4$ is interesting as a host crystal of rare-earth-activated phosphors because it has excellent thermal and optical properties [8–10].

In general, the deposition of transparent thin films on flat substrates causes optical effects due to different refractive indices, and hence optical paths [11]. Fresnel reflection occurs at the air/film interface, where the reflectance depends directly on the refractive index of thin films. When applying $CaMoO_4$ to thin-film phosphors, its high refractive index (1.98–2.00) [10,12] gives the reflectance of approximately 11% at the film surface against the incident light. The light emitted from thin-film phosphors is also influenced by reflection, which has already been a major problem in light-emitting semiconductor devices [13]. That is, the emitted light propagating in high-refractive-index thin films undergoes total internal reflection (the so-called waveguide mode). A large part of the emitted light is then trapped in thin films, and is not well extracted from the surface to the air. In the case of $CaMoO_4$, the critical angle for total reflection is 30.2°, and only 6.8% of the emitted light can be extracted.

The design of film structures to diminish unnecessary reflection is key for achieving high luminescence intensity in thin-film phosphors. Relevant structures are similar to those of antireflective (AR) coatings. Moth-eye mimicking structures have been successfully employed as AR coatings

in optical devices including solar cells [14,15] and light-emitting diodes [16,17]. Multifunctional moth-eye type coatings have also been developed for thermochromic/hydrophobic smart window applications [18]. A sol–gel method is promising for fabricating moth-eye type AR coatings. For example, alumina-based AR coatings were prepared on glass or polymer substrates by the combination of the sol–gel dip-coating method and the hot water treatment [19–21]. The surface morphology of dip-coated alumina films was changed by the hot water treatment to give a flowerlike structure consisting of nanocrystals. The resultant alumina films were demonstrated to work as moth-eye-type AR coatings. This method could be applied to the fabrication of luminescent AR coatings in our previous study [22]. A similar sol–gel coating was also made on thermochromic VO_2 films to enhance optical transmittance [23].

In the present work, we introduced a nanocomposite structure in which silver nanoparticles were dispersed in a phosphor matrix consisting of crystalline $CaMoO_4$:Eu^{3+} and amorphous alumina to create luminescent AR coatings. Silver nanoparticles were expected to enhance luminescence due to the surface plasmon resonance (SPR) effect [24] and/or the light scattering effect. Amorphous alumina was necessary to modulate the film morphology by the hot water treatment. The obtained $CaMoO_4$:Eu^{3+}/Ag coatings exhibited better luminescence properties than Ag-free $CaMoO_4$:Eu^{3+} coatings without losing the AR property.

2. Materials and Methods

Four kinds of thin films (Film-A1, B1, C1, and D1) were fabricated by the sol–gel method. A standard solution for coating was prepared as follows. 0.143 mmol of $(NH_4)_6Mo_7O_{24}\cdot 4H_2O$ (99.0%, Wako Pure Chemical Industries, Osaka, Japan) and 2.00 mmol of citric acid (98.0%, Wako) were dissolved in 7.5 mL of ethanol (99%, Amakasu Chemical Industries, Tokyo, Japan). Then, 0.95 mmol of $Ca(NO_3)_2\cdot 4H_2O$ (99.9%, Wako), 0.05 mmol of $Eu(NO_3)_3\cdot 6H_2O$ (99.95%, Wako), and 1.00 mmol of $Al(NO_3)_3\cdot 9H_2O$ (99.9%, Wako) were further dissolved in the above solution, giving a cation molar ratio of Ca^{2+}:Eu^{3+}:Mo^{6+}:Al^{3+} = 0.95:0.05:1:1. Then, 1.2 g of polyethylene glycol (PEG10000, Merck, Tokyo, Japan) and 2.5 mL of deionized water were added to the solution, followed by stirring for 1 h at room temperature. The resultant transparent solution was dip-coated on a silica glass substrate 1 mm in thickness (Monotech, Saitama, Japan) at a withdrawal speed of 0.4 mm s^{-1}. The coated substrate was dried at 90 °C for 15 min using a drying oven and then annealed at 700 °C for 1 h in air using a muffle furnace. The coating, drying, and annealing procedures were repeated two additional times to obtain Film-A1.

In the next experiment, 0.05 mmol of $AgNO_3$ (99.8%, Wako) was added to the above standard solution at the time of addition of PEG10000 and deionized water. The resultant solution was coated on the silica glass substrate in the same way to obtain Film-B1. It should be mentioned that the amount of $AgNO_3$ had been optimized in terms of the film microstructure. An excess amount (for example, 0.10 mmol) of $AgNO_3$ led to the formation of a porous thin film.

In Film-C1 and D1, silver colloid nanoparticles which were prepared by the methods described in the literature [25,26] were introduced to the film fabrication process. $AgNO_3$ (9 mg) was dissolved in 49 mL of deionized water under vigorous stirring at a temperature of 90 °C. Then, 1 mL of a 38.8 mM aqueous solution of trisodium citrate (99.0%, Wako, prepared separately) was added to the $AgNO_3$ solution kept at 90 °C. The resultant solution was reacted at 90 °C under refluxing and vigorous stirring for 90 min, followed by cooling naturally to room temperature. A silver colloidal solution was obtained after removing larger silver particles precipitated in the solution by centrifuging at 500 rpm for 30 min. Finally, a volume of the silver colloidal solution was adjusted to 50 mL by adding deionized water.

In preparing a coating solution for Film-C1, 2.5 mL of deionized water was replaced with the same volume of the silver colloidal solution at the time of addition of PEG10000 and deionized water in the above standard solution. Film-D1 was fabricated by combining the procedures for Film-B1 and C1. That is, 0.05 mmol of $AgNO_3$ was added to the coating solution of Film-C1 at the time of

addition of PEG10000 and the silver colloidal solution. The coating, drying, and annealing procedures for Film-C1 and D1 were the same as those for Film-A1.

The hot water treatment for the above-obtained film samples was carried out by immersing Film-A1, B1, C1, or D1 in 10 mL of deionized water at 80 °C for 30 min. The treated film samples were washed with deionized water and acetone and dried at room temperature to obtain, in sequence, Film-A2, B2, C2, or D2.

Crystal structures of the samples obtained were identified by an X-ray diffraction (XRD) analysis with a D8-02 diffractometer (Bruker AXS, Yokohama, Japan) using CuKα radiation. Optical transmission and absorption spectra of the samples were recorded with a V-670 ultraviolet (UV)-visible spectrophotometer (JASCO, Hachioji, Japan). Photoluminescence (PL) spectra of the samples were measured at room temperature with an FP-6500 spectrofluorophotometer (JASCO) using a xenon lamp (150 W) as a light source. The film samples were mounted directly on the attachment in the PL measurement. A filter was used to remove a second-order peak of the excitation light. The microstructure of the samples was observed by field emission scanning electron microscopy (FESEM) with an S-4700 microscope (Hitachi, Tokyo, Japan). Transmission electron microscopy (TEM) was also carried out to observe the silver colloid nanoparticles with a TECNAI F20 microscope (Philips/FEI, Hillsboro, OR, USA).

3. Results and Discussion

3.1. Effect of Hot Water Treatment

Figure 1a shows XRD patterns of Film-A1 (before the hot water treatment) and A2 (after the hot water treatment). The respective patterns have a broad amorphous halo at 2θ = 22°, coming from the silica glass substrate. Small peaks appearing at 2θ = 28.8° in both patterns correspond to the strongest (112) peak in the powder pattern of the tetragonal $CaMoO_4$ phase (ICDD 029-0351). To further confirm the crystallization of $CaMoO_4$, the coating solution for Film-A1 was dried at 60 °C for 3 days and then annealed at 700 °C for 3 h in air (denoted as Powder-A1). The XRD pattern of Powder-A1 (Supplementary Materials, Figure S1) clearly shows diffraction peaks, all of which are assigned to the tetragonal $CaMoO_4$ phase. The annealing temperature of 700 °C is therefore enough for the crystallization of $CaMoO_4$. Additionally, no peaks due to aluminum-containing compounds were seen in the XRD pattern of Powder-A1, although the solution contained a considerable amount of $Al(NO_3)_3 \cdot 9H_2O$. This result coincides with that reported previously for the aluminum-added YVO_4:Bi^{3+}, Eu^{3+} films and powders [22]. That is, the heat treatment of the solution containing all the metal sources led to the crystallization of YVO_4:Bi^{3+}, Eu^{3+}, and simultaneously, the formation of amorphous Al_2O_3. As such, the phase separation is crucial for the morphological change of the samples by the hot water treatment.

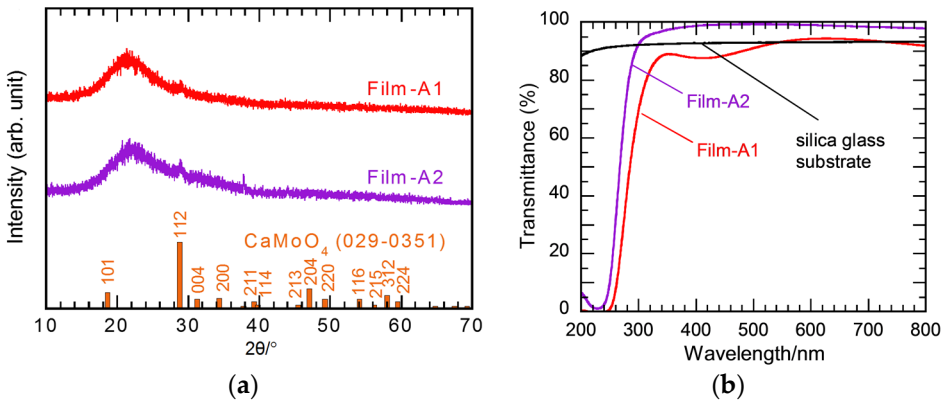

Figure 1. *Cont.*

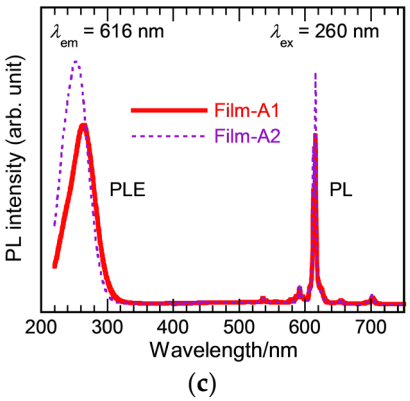

Figure 1. Film A1 (before the hot water treatment) and A2 (after the hot water treatment). (**a**) XRD patterns; (**b**) optical transmission spectra; (**c**) photoluminescence (PL) excitation and emission spectra.

It appears that the XRD pattern is not much changed for Film-A2 after the hot water treatment. In contrast, the XRD pattern of Powder-A2, which was obtained by immersing 0.05 g of Powder-A1 in 10 mL of deionized water at 80 °C for 1 h, had higher background noise (Figure S1). This is probably due to the partial fragmentation of particles consisting of crystalline $CaMoO_4$ and amorphous Al_2O_3 during the hot water treatment. The effect of the hot water treatment will be discussed later in detail.

The optical properties of Film-A1 and A2 were evaluated to see the effect of the hot water treatment. Figure 1b shows the optical transmission spectra of Film-A1 and A2, together with that of the silica glass substrate as a reference. Film-A1 has more than 80% transmittance in the visible light region due to its microstructure with a flat surface and a uniform thickness, as shown later. The optical absorption of $CaMoO_4$ is associated with the O^{2-}–Mo^{6+} charge transfer (CT) transition within the MoO_4 units [5]. The apparent energy gap between the O 2*p* valence band and the Mo 4*d* conduction band is reportedly located in the range of 4.28–4.86 eV, depending on the sample preparation condition [8]. A sudden decrease in the transmittance of Film-A1 is therefore caused by the CT absorption of $CaMoO_4$, which also supports its crystallization in the thin film. After the hot water treatment, Film-A2 exhibits an AR effect with enhanced transmittance. As a comparative study, thin-film samples were prepared from the standard coating solution, from which $Al(NO_3)_3{\cdot}9H_2O$ was eliminated, similarly to Film-A1 and A2. According to the XRD analysis, the resultant films were crystallized as $CaMoO_4$. However, the transmittance spectra were not much changed before and after the hot water treatment (Figure S2), thereby indicating of the effectiveness of the aluminum addition to the film samples.

Another important issue is whether the observed AR effect is due to the homogeneously increased porosity or the gradually changed density of the film. We then investigated an angular dependence of the optical transmittance of Film-A1 and A2. Figure S3 shows results for p-polarized and s-polarized light with five incidence angles between 0° and 60°. Transmittance of Film-A1 for p-polarized light increases with increasing the incidence angle up to 45°, which is attributed to a decrease in the reflectance of p-polarized light up to the Brewster's angle. In contrast, the transmittance spectra of Film-A2 are almost independent of incidence angle for p-polarized light. For s-polarized light, Film-A1 shows a large decrease of the transmittance with increasing incidence angle, indicative of the increased reflection. Film-A2 keeps higher transmittance against the varied incidence angle. This smaller angular dependence of transmittance is a typical feature of films having a graded refractive index.

PL excitation and emission spectra of Film-A1 and A2 are shown in Figure 1c. Upon excitation at a wavelength of 260 nm, Film-A1 and A2 exhibit characteristic line emissions in the red region. These emissions are ascribed to electronic transitions in Eu^{3+} ions. When doped in the $CaMoO_4$ host crystal, Eu^{3+} would occupy the Ca^{2+} site surrounded by eight oxygens. Although the CaO_8 units have two different Ca–O distances (0.2459 and 0.2471 nm) [27], the Ca^{2+} site in pure $CaMoO_4$ reportedly

has inversion symmetry [28]. The Eu^{3+} ions located in the site with inversion symmetry would give only a weak emission due to the magnetic-dipole $^5D_0$–$^7F_1$ transition at around 591 nm [29]. However, the emission at 616 nm—attributed to the forced electric-dipole $^5D_0$–$^7F_2$ transition—is much stronger than the other emissions in the present film samples, as seen in Figure 1c. This result may imply that the Eu^{3+} ions are located in the site without inversion symmetry. A similar phenomenon has been observed in many $CaMoO_4$:Eu^{3+} samples, as reported in the literature [9,28,30]. One possible explanation for this discrepancy is given by considering the polarizability effect of the MoO_4 units on the EuO_8 units [28]. That is, the extent of the polarizability around the Eu^{3+} ions in the EuO_8 units is increased by the neighboring MoO_4 units in $CaMoO_4$:Eu^{3+}. This changes the crystal field of EuO_8, and hence the transition probability of the Eu^{3+} ions. The PL excitation spectra have a broad band ranging between approximately 200 and 300 nm. This band results from the overlapping of the O^{2-}–Mo^{6+} and the O^{2-}–Eu^{3+} CT transition.

It is also clearly seen from Figure 1c that the PL intensity of Film-A2 is higher than that of Film-A1. Because the amount of the luminescent $CaMoO_4$:Eu^{3+} phase in the film sample is not increased by the mere hot water treatment at 80 °C for 30 min, the enhanced PL property of Film-A2 should be related to the change in the optical property, as seen in Figure 1b. That is, the AR effect against the external, incident light also works on the internal, emitted light. The efficiency of light extraction from the film surface is improved in this case.

3.2. Effect of Silver Addition

The silver colloid nanoparticles used for fabricating Film-C1 and D1 are characterized first. Figure 2a,b shows an XRD pattern and a TEM image, respectively, of the nanoparticles. A broad amorphous halo at $2\theta = 22°$ in Figure 2a is due to the glass holder for the XRD measurement. The appearance of a peak at $2\theta = 38.1°$ clearly indicates the formation of silver (XRD; ICDD 04-0783). An average particle size of silver is 50 nm as seen in Figure 2b. An absorption spectrum of the silver colloidal solution—which was diluted four times—indicates the occurrence of SPR, as shown in Figure 2c. The absorption wavelength due to SPR of silver depends on the size of the nanoparticles [31]. The observed absorption wavelengths—peaking at 450 nm—correspond to the size of 50–60 nm in the size–wavelength relationship for SPR of silver. The silver colloid nanoparticles are well dispersed in water (as seen in Figure 2d), which is due to the presence of the citrate ions working as the capping agent [26].

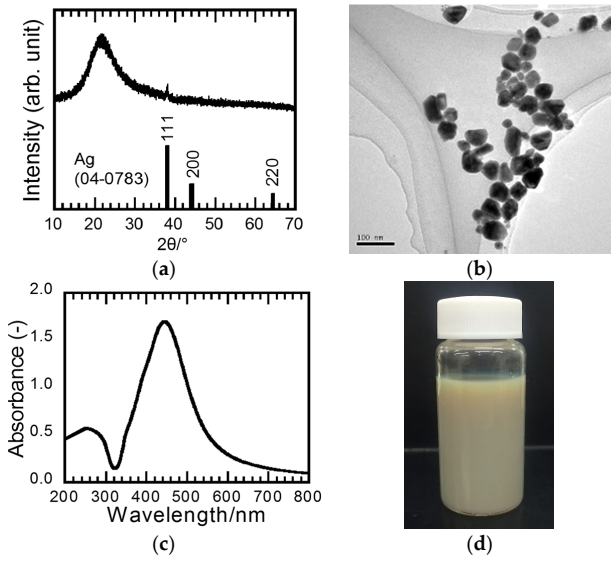

Figure 2. Silver colloid nanoparticles. (**a**) XRD pattern; (**b**) TEM image; (**c**) optical absorption spectrum; (**d**) optical image.

Figure 3a compares XRD patterns of Film-A1, B1, C1, and D1. The appearance of the (112) peak at 2θ = 28.8° in all patterns confirms the crystallization of the $CaMoO_4$ phase in these films. The addition of silver in Film-B1, C1, and D1 did not seem to influence the crystallization behavior. This was further examined with powders obtained by drying the respective coating solutions at 60 °C for 3 days and annealing at 700 °C for 3 h in air (denoted as Powder-B1, C1, and D1). In fact, the crystallization of $CaMoO_4$ is not influenced by the silver addition, as indicated by the similar XRD patterns in Figure S4. The presence of silver could also be confirmed by the appearance of the small (111) peak of Ag in Powder-C1 and D1 derived from the solutions containing the silver colloid nanoparticles.

After the hot water treatment, Film-B2, C2, and D2 still have the (112) peak of the $CaMoO_4$ phase in the XRD pattern, similarly to Film-A2 in Figure 3b. The silver addition does not greatly influence the crystalline state of the films during the hot water treatment.

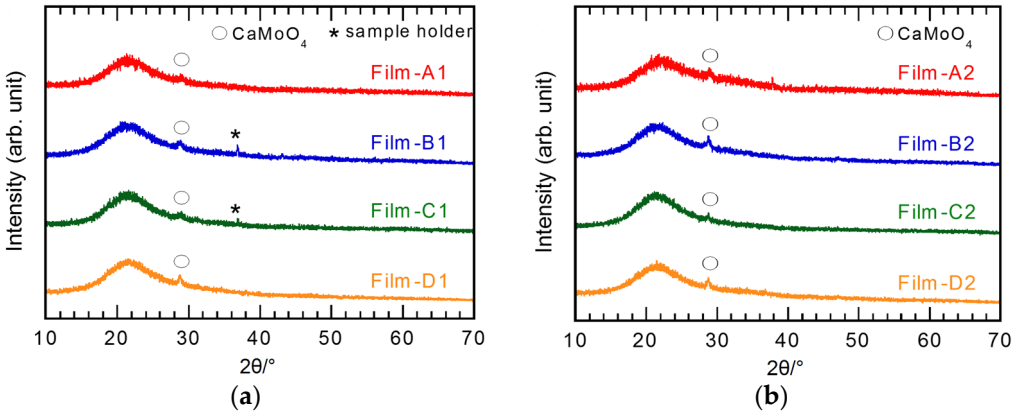

Figure 3. XRD patterns of films. (**a**) Film-A1, B1, C1, and D1 before the hot water treatment; (**b**) Film-A2, B2, C2, and D2 after the hot water treatment.

Morphology of the films is shown in Figure 4 andFigure 5 as surface and cross-section FESEM images. The films before the hot water treatment had a flat and smooth surface and a uniform thickness (Figure 4). From the cross-section images, the film thickness was observed to be 270 (Film-A1), 280 (B1), 300 (C1), and 230 nm (D1). In Film-D1, tiny precipitates approximately 50 nm in size were also observed as white spots on the film surface. Together with the XRD results of the powders, the precipitates are thought to be the silver nanoparticles contained in the coating solution.

After the hot water treatment, the surface morphology was drastically changed to disordered nanostructures in all the films (Figure 5). Because the $CaMoO_4$ phase does not react with water, the observed change was brought by the reaction between the amorphous aluminum-containing compounds and water promoted at the temperature of 80 °C. This phenomenon has been known to occur in the sol–gel-derived alumina gel films through the dissolution–reprecipitation process [19–21]. In the composite films consisting of the aluminum-containing compounds and the other crystalline phase, the former undergo the reaction to give the morphological change to the entire films. Following this change, the film thickness was increased to 620 (Film-A2), 680 (B2), 540 (C2), and 500 nm (D2). In the depth direction, the reaction seemed to be limited to the film surface and the region near the film/substrate interface was not much changed. This would generate a continuous decrease in the film density and accordingly the refractive index towards the surface, which could explain the above-mentioned AR effect in Film-A2 as shown in Figure 1b.

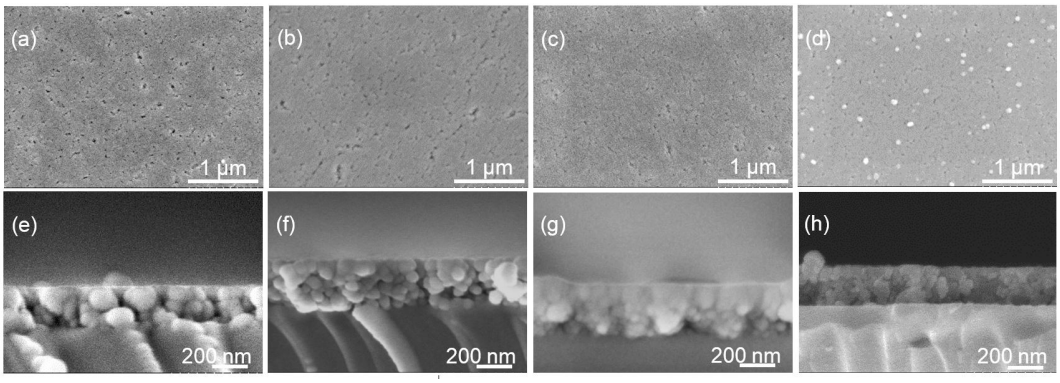

Figure 4. Surface (top) and cross-section (bottom) field emission SEM (FESEM) image. (**a,e**) Film-A1; (**b,f**) Film-B1; (**c,g**) Film-C1; (**d,h**) Film-D1.

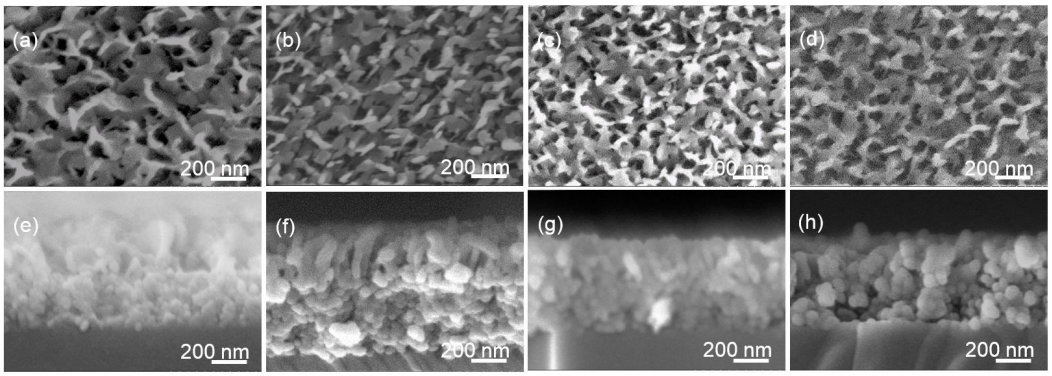

Figure 5. Surface (top) and cross-section (bottom) FESEM image. (**a,e**) Film-A2; (**b,f**) Film-B2; (**c,g**) Film-C2; (**d,h**) Film-D2.

Figure 6a shows optical transmission spectra of Film-B1, C1, and D1, together with those of Film-A1 and the silica glass substrate. Film-B1 and C1 have more than 80% transmittance in the visible light region. They also exhibit an interference pattern due to the high refractive index of the films. Because of the composite structure, the actual refractive index of the films should be between 2.00 (crystalline $CaMoO_4$) [10,12] and 1.645 (amorphous Al_2O_3) [32]. A larger decrease of the transmittance of Film-D1 was caused by the SPR absorption and/or the light scattering by the silver nanoparticles. It was confirmed that the transmittance increases and the interference disappears in the films after the hot water treatment (Film-B2, C2, and D2 in Figure 6b). It is also noticed that the transmittance of Film-C2 and D2—which originate from the solutions containing the silver colloid nanoparticles—was lower than that of Film-A2 and B2 in the shorter wavelength range. The SPR absorption and/or the light scattering by the silver nanoparticles may become obvious in Film-C2 and survive in Film-D2 after the hot water treatment.

Figure 7 shows PL excitation and emission spectra of Film-A2, B2, C2, and D2. The spectral structure of both the excitation and the emission spectra was not changed for Film-B2, C2, and D2, as compared to Film-A2. Therefore, the silver addition did not disturb the electronic transitions of the Eu^{3+} ions doped in the $CaMoO_4$ phase. The PL intensity of Film-B2 was almost the same as that of Film-A2. This indicates that the addition of $AgNO_3$ to the coating solution was not effective in changing the optical properties (the transmission in Figure 6b and the emission in Figure 7b) of the finally obtained film. In contrast, the PL intensity was enhanced slightly in Film-C2 (10% increase), and remarkably in Film-D2 (50% increase). Because the transmittance of the films in the emission wavelength region around 616 nm is not very different, the PL enhancement is considered to be due to the SPR effect on the emission and/or the light scattering effect on the excitation. The SPR

effect is based on the energy transfer from the silver nanoparticles to the Eu^{3+} ions or the local field enhancement around the silver nanoparticles and the Eu^{3+} ions [24,33], leading to the increase in the PL intensity. It is necessary to perform the time-resolved PL measurement to ensure the SPR effect, which is our next subject. The light scattering effect is related to Rayleigh scattering of the excitation light by the silver nanoparticles inside the films, which may increase the opportunity for the excitation. Although it is not clear which effect is dominant, the introduction of the silver nanoparticles has been demonstrated to be beneficial for fabricating highly transparent luminescent coatings.

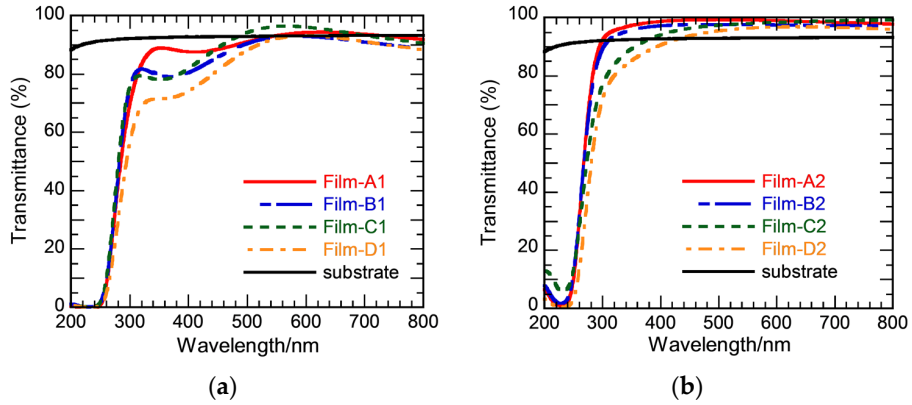

Figure 6. Optical transmission spectra of films. (**a**) Film-A1, B1, C1, and D1 before the hot water treatment; (**b**) Film-A2, B2, C2, and D2 after the hot water treatment.

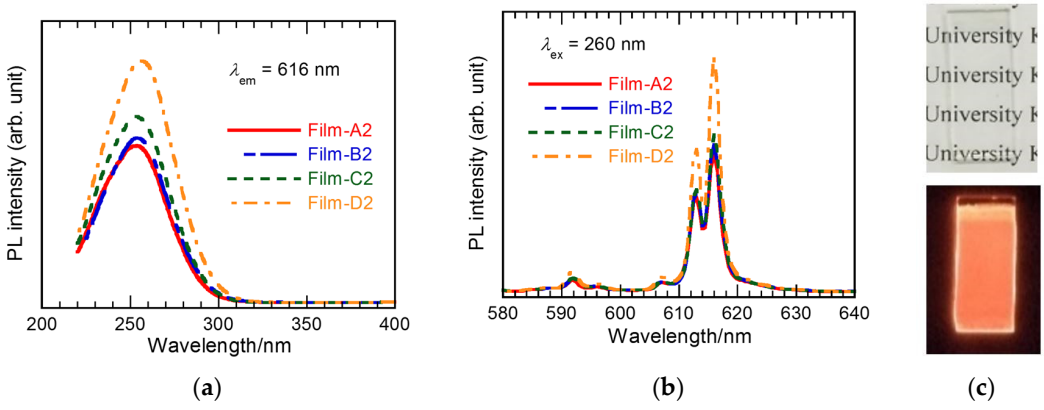

Figure 7. PL properties of films after the hot water treatment. (**a**) PL excitation spectra; (**b**) PL emission spectra; (**c**) appearance of Film-D2 under the fluorescent lamp (top) and the UV lamp (bottom).

4. Conclusions

Luminescent AR coatings were fabricated on silica glass substrates by the sol–gel dip coating technique and subsequent hot water treatment. The films were composed of a crystalline $CaMoO_4$:Eu^{3+} phase and an amorphous Al_2O_3 phase. The films underwent a significant morphological change due to the reaction between the Al_2O_3 phase and water during the hot water treatment. This brought the AR effect and simultaneously with the luminescence enhancement. The addition of Ag nanoparticles to the films further increased the luminescence intensity. Thus, we could obtain highly transparent and luminescent nanocomposite AR coatings.

Supplementary Materials: The following are available online at http://www.mdpi.com/2079-6412/7/6/73/s1. Figure S1: XRD patterns of Powder-A1 and A2; Figure S2: Optical transmission spectra of Film-A'1 and A'2; Figure S3: Incidence-angle dependence of optical transmission spectra of Film-A1 and A2; Figure S4: XRD patterns of Powder-B1, C1, and D1.

Acknowledgments: This study was supported by JSPS KAKENHI Grant Number 25420715.

Author Contributions: Kazuhiro Matsumoto performed the experiments; Manabu Hagiwara discussed the results; Shinobu Fujihara supervised the work; Kazuhiro Matsumoto and Shinobu Fujihara wrote the paper.

Conflicts of Interest: The authors declare no conflict of interest.

References

1. Chen, X.Y.; Zhang, Z.J.; Zhu, L.L.; Xu, M.; Wang, H.; Li, A.G.; Zhao, J.T. Preparation, and characterizations of a novel luminescence Lu_2WO_6:Eu^{3+} film as potential scintillator. *Appl. Surf. Sci.* **2014**, *317*, 730–736. [CrossRef]
2. Huang, X.; Han, S.; Huang, W.; Liu, X. Enhancing solar cell efficiency: the search for luminescent materials as spectral converters. *Chem. Soc. Rev.* **2013**, *42*, 173–201. [CrossRef] [PubMed]
3. Kim, J.; Miyokawa, N.; Ide, K.; Hiramatsu, H.; Hosono, H.; Kamiya, T. Transparent amorphous oxide semiconductor thin film phosphor, In–Mg–O:Eu. *J. Ceram. Soc. Jpn.* **2016**, *124*, 532–535. [CrossRef]
4. Kyomen, T.; Hanaya, M.; Takashima, H. Electroluminescence near interfaces between (Ca,Sr)TiO_3:Pr phosphor and SnO_2:Sb transparent conductor thin films prepared by sol–gel and spin-coating methods. *J. Lumin.* **2014**, *149*, 133–137. [CrossRef]
5. Zhang, Y.; Holzwarth, N.A.W.; Williams, R.T. Electronic band structures of the scheelite materials $CaMoO_4$, $CaWO_4$, $PbMoO_4$, and $PbWO_4$. *Phys. Rev. B* **1998**, *57*, 12738–12750. [CrossRef]
6. Thongtem, T.; Kungwankunakorn, S.; Kuntalue, B.; Phuruangrat, A.; Thongtem, S. Luminescence and absorbance of highly crystalline $CaMoO_4$, $SrMoO_4$, $CaWO_4$ and $SrWO_4$ nanoparticles synthesized by co-precipitation method at room temperature. *J. Alloys Compd.* **2010**, *506*, 475–481. [CrossRef]
7. Bonner, G.M.; Pask, H.M.; Lee, A.J.; Kemp, A.J.; Wang, J.; Zhang, H.; Omatsu, T. Measurement of thermal lensing in a CW $BaWO_4$ intracavity Raman laser. *Opt. Express* **2012**, *20*, 9810–9818. [CrossRef] [PubMed]
8. De Azevedo Marques, A.P.; Longo, V.M.; de Melo, D.M.A.; Pizani, P.S.; Leite, E.R.; Varela, J.A.; Longo, E. Shape controlled synthesis of $CaMoO_4$ thin films and their photoluminescence property. *J. Solid State Chem.* **2008**, *181*, 1249–1257. [CrossRef]
9. Raju, G.S.R.; Pavitra, E.; Ko, Y.H.; Yu, J.S. A facile and efficient strategy for the preparation of stable $CaMoO_4$ spherulites using ammonium molybdate as a molybdenum source and their excitation induced tunable luminescent properties for optical applications. *J. Mater. Chem.* **2012**, *22*, 15562–15569. [CrossRef]
10. Dutta, S.; Som, S.; Sharma, S.K. Excitation spectra and luminescence decay analysis of K^+ compensated Dy^{3+} doped $CaMoO_4$ phosphors. *RSC Adv.* **2015**, *5*, 7380–7387. [CrossRef]
11. Pulker, H.K. *Coatings on Glass*, 2nd ed.; Elsevier: Amsterdam, The Netherlands, 1999; pp. 433–440.
12. Cavalli, E.; Bovero, E.; Belletti, A. Optical spectroscopy of $CaMoO_4$:Dy^{3+} single crystals. *J. Phys. Condens. Matter* **2002**, *14*, 5221–5228. [CrossRef]
13. Zheng, Q.; Zhang, D.; Huang, J.; Wang, Y.; Huang, F. Integrating surface textures on ZnO substrate for high light extraction efficiency light-emitting diode. *J. Phys. Chem. C* **2014**, *118*, 14894–14898. [CrossRef]
14. Yang, J.; Luo, F.; Kao, T.S.; Li, X.; Ho, G.W.; Teng, J.; Luo, X.; Hong, M. Design and fabrication of broadband ultralow reflectivity black Si surfaces by laser micro/nanoprocessing. *Light Sci. Appl.* **2014**, *3*, e185. [CrossRef]
15. Leem, J.W.; Kim, S.; Lee, S.H.; Rogers, J.A.; Kim, E.; Yu, J.S. Efficiency enhancement of organic solar cells using hydrophobic antireflective inverted moth-eye nanopatterned PDMS films. *Adv. Energy Mater.* **2014**, *4*, 1301315. [CrossRef]
16. Kasugai, H.; Nagamatsu, K.; Miyake, Y.; Honshio, A.; Kawashima, T.; Iida, K.; Iwaya, M.; Kamiyama, S.; Amano, H.; Akasaki, I.; et al. Light extraction process in moth-eye structure. *Phys. Status Solidi c* **2006**, *3*, 2165–2168. [CrossRef]
17. Rao, J.; Winfield, R.; Keeney, L. Moth-eye-structured light-emitting diodes. *Opt. Commun.* **2010**, *283*, 2446–2450. [CrossRef]
18. Qian, X.; Wang, N.; Li, Y.; Zhang, J.; Xu, Z.; Long, Y. Bioinspired multifunctional vanadium dioxide: Improved thermochromism and hydrophobicity. *Langmuir* **2014**, *30*, 10766–10771. [CrossRef] [PubMed]
19. Yamaguchi, N.; Tadanaga, K.; Matsuda, A.; Minami, T.; Tatsumisago, M. Anti-reflective coatings of flowerlike alumina on various glass substrates by the sol–gel process with the hot water treatment. *J. Sol-Gel Sci. Technol.* **2005**, *33*, 117–120. [CrossRef]

20. Tadanaga, K.; Yamaguchi, N.; Uraoka, Y.; Matsuda, A.; Minami, T.; Tatsumisago, M. Anti-reflective properties of nano-structured alumina thin films on poly(methyl methacrylate) substrates by the sol–gel process with hot water treatment. *Thin Solid Films* **2008**, *516*, 4526–4529. [CrossRef]
21. Tadanaga, K. Surface morphology control of thin films prepared by solution processes and its application. *J. Ceram. Soc. Jpn.* **2013**, *121*, 819–824. [CrossRef]
22. Tanaka, S.; Fujihara, S. Luminescent antireflective coatings with disordered surface nanostructures fabricated by liquid processes. *Langmuir* **2011**, *27*, 2929–2935. [CrossRef] [PubMed]
23. Liu, C.; Wang, N.; Long, Y. Multifunctional overcoats on vanadium dioxide thermochromic thin films with enhanced luminous transmission and solar modulation, hydrophobicity and anti-oxidation. *Appl. Surf. Sci.* **2013**, *283*, 222–226. [CrossRef]
24. Pillonnet, A.; Berthelot, A.; Pereira, A.; Benamara, O.; Derom, S.; des Francs, G.C.; Jurdyc, A.-M. Coupling distance between Eu^{3+} emitters and Ag nanoparticles. *Appl. Phys. Lett.* **2012**, *100*, 153115. [CrossRef]
25. Lee, P.C.; Meisel, D. Adsorption and surface-enhanced Raman of dyes on silver and gold sols. *J. Phys. Chem.* **1982**, *86*, 3391–3395. [CrossRef]
26. Sharma, V.K.; Yngard, R.A.; Lin, Y. Silver nanoparticles: green synthesis and their antimicrobial activities. *Adv. Colloid Interf. Sci.* **2009**, *145*, 83–96. [CrossRef] [PubMed]
27. Gürmen, E.; Daniels, E.; King, J.S. Crystal structure refinement of $SrMoO_4$, $SrWO_4$, $CaMoO_4$, and $BaWO_4$ by neutron diffraction. *J. Chem. Phys.* **1971**, *55*, 1093–1097. [CrossRef]
28. Parchur, A.K.; Ningthoujam, R.S.; Rai, S.B.; Okram, G.S.; Singh, R.A.; Tyagi, M.; Gadkari, S.C.; Tewari, R.; Vatsa, R.K. Luminescence properties of Eu^{3+} doped $CaMoO_4$ nanoparticles. *Dalton Trans.* **2011**, *40*, 7595–7601. [CrossRef] [PubMed]
29. Blass, G.; Grabmaier, B.C. *Luminescent Materials*; Springer-Verlag: Berlin, Germany, 1994; pp. 41–44.
30. Laguna, M.; Nuñez, N.O.; Becerro, A.I.; Ocaña, M. Morphology control of uniform $CaMoO_4$ microarchitectures and development of white light emitting phosphors by Ln doping (Ln = Dy^{3+}, Eu^{3+}). *CrystEngComm* **2017**, *19*, 1590–1600. [CrossRef]
31. Paramelle, D.; Sadovoy, A.; Gorelik, S.; Free, P.; Hobley, J.; Fernig, D.G. A rapid method to estimate the concentration of citrate capped silver nanoparticles from UV-visible light spectra. *Analyst* **2014**, *139*, 4855–4861. [CrossRef] [PubMed]
32. Nayar, P.; Khanna, A. Optical properties and thermal stability of alumina films grown by pulsed laser deposition. *Eur. Phys. J. Appl. Phys.* **2013**, *64*, 10301. [CrossRef]
33. Eihelbaum, M.; Rademann, K. Plasmonic enhancement or energy transfer? On the luminescence of gold-, silver-, and lanthanide-doped silicate glasses and its potential for light-emitting devices. *Adv. Funct. Mater.* **2009**, *19*, 2045–2052. [CrossRef]